Supplementary Information

for

Ice loss in High Mountain Asia and the Gulf of Alaska observed by CryoSat-2 swath altimetry between 2010 and 2019

Livia Jakob, Noel Gourmelen, Martin Ewart, Stephen Plummer

Here we provide supplementary information about:

- Quality thresholds used for data processing
- Handling of missing data
- Uncertainty assessment
- Supplementary figures and tables

1 Supplementary information about data processing and methodology

1.1 Quality weights for *dh/dt*

When generating time-dependent elevation changes we use weights, based on attributes (power and coherence) to penalise lower quality measurements. We use the following formula to calculate a quality rating (see Gourmelen et al., 2018),

$$w_v = \frac{v^2}{\max\left(v_{i=1}^{n}\right)^2}, \quad (1)$$

where v is an attribute value (either power or coherence) and w_v the attribute weight rating. We then average the weight ratings to retrieve a single quality weight for each measurement.

1.2 Quality for *dh/dt* bins

We remove bins that exceed a set of quality criteria. As described in the corresponding paper we calculate a 30-day surface elevation time series for each bin, which is used as an additional check of the *dh/dt* quality of a bin (note that the rate of change of each bin is calculated fitting all the *elevDiff* [1] measurements and not based on the time series). To remove low quality bins from the results we define a set of minimal thresholds:

(1) Elevation change uncertainties: Bins with uncertainties higher than 1 m yr^{-1} are excluded.

[1] *elevDiff* describes the elevation differences between the TanDEM-X 90m DEM (German Aerospace Center [DLR], 2018) and the swath elevation measurements, i.e. topography is removed.

(2) Temporal completeness: We used the degree of completeness of the corresponding time series to exclude bins with a number of 30-day periods that did not show any measurements. Bins with less than 60% temporal coverage were excluded.

(3) Interannual change: The standard deviation of the corresponding time series (with the rate removed) was used to exclude bins with unrealistically high interannual change. Bins with a standard deviation higher than 10 were excluded.

1.3 Filling gaps with hypsometric averaging

Our hypsometric model makes use of the relation between elevation and *dh/dt* to extrapolate rates of elevation change (Moholdt et al., 2010a, 2010b; Nilsson et al., 2015). For each sub-region we calculate time-dependent rates of elevation changes in 100m elevation bands. We use the RGI 6.0 second order regions (RGI Consortium, 2017), containing sub-regions sufficiently large to retrieve enough measurements per elevation band. We fit one to three order polynomials to the relation between elevation and *dh/dt*, where the order of the polynomial was decided based on iterative increase of the polynomial order until the adjusted R^2 coefficient stabilised (Nilsson et al., 2015). In addition, subjective judgement was used to avoid runaway tails (Nuth et al., 2010). The elevation dependent *dh/dt* curves, fitted polynomials and hypsometry functions for each sub-region are shown in Figure 6 and Figure 11 in the paper.

For each 100 m elevation band k we calculate the rate of change $\Delta h(k)$ based on the fitted polynomials and multiply it with the glacierised area of the band $A(k)$ to extract volume change $V(k)$. $A(k)$ is retrieved for each elevation band using the TanDEM-X DEM and the RGI 6.0 glacier masks. The sum of all $V(k)$ represents the total volume change rate in a bin or region.

1.4 Uncertainty assessment

The error budget on mass change has three uncertainty sources, which are assumed to be independent and uncorrelated: uncertainty on time-dependent elevation change ($\sigma_{\Delta h}$), uncertainty on glacierised area (σ_A) and uncertainty on mass-volume conversion (σ_p).

The rate of change uncertainty for each 100 x 100 km bin is based on the standard error of the regression model. We conservatively use a factor of five (Berthier et al., 2014; Brun et al., 2017) for uncertainties on areas without coverage of swath measurements:

$$\sigma_{\Delta h} = \sigma_{\Delta z}(g + 5u)\,, \qquad (2)$$

where g is the proportional coverage of glacierised area at 400-metre postings, u is $(1 - g)$ and $\sigma_{\Delta z}$ is the standard error of the regression. To account for errors due to temporal changes in glacier extents and polygon digitization (Shean et al., 2020) we use an error of 10% ($\sigma_A = 0.1A$) on the glacierised area A in a bin, even though the reported uncertainty of the RGI is ~8%

(Pfeffer et al., 2014). Assuming independence between the two error components ($\sigma_A, \sigma_{\Delta h}$), volume change uncertainty ($\sigma_{\Delta V}$) of a bin is:

$$\sigma_{\Delta V} = \sqrt{(\sigma_{\Delta h}\, A)^2 + (\sigma_A\, \Delta h)^2}\,, \tag{3}$$

where Δh is the elevation change rate of the respective bin. To retrieve the volume change uncertainty on extrapolated bins (using the hypsometric averaging method) we fit a second order polynomial ($\sigma_{\Delta h}(k) = ak^2 + bk + c$) to the relation between rate uncertainty and elevation for each region (see Table S2, Table S3). For each 100 m elevation band k within a bin we extract $\sigma_{\Delta h}(k)$ and apply Eq. (3) to calculate $\sigma_{\Delta V}(k)$. The aggregated volume change uncertainty of an extrapolated bin is calculated as the quadratic sum of the uncertainties of each elevation band.

To generate the region-wide volume uncertainty ($\sigma_{\Delta V_{tot}}$) we combine all the values (including extrapolated bins) in quadrature. We use a density uncertainty of $\sigma_p = 60$ kg m^{-3}, and a density mass conversion of p = 850 kg m^{-3} (Huss, 2013). The total mass balance is:

$$\sigma_{\Delta M_{tot}} = \sqrt{(\sigma_{\Delta V_{tot}}\, p)^2 + (\sigma_p\, \Delta V_{tot})^2}\,, \tag{4}$$

where ΔV_{tot} is the total volume change for the region.

2 Supplementary figures

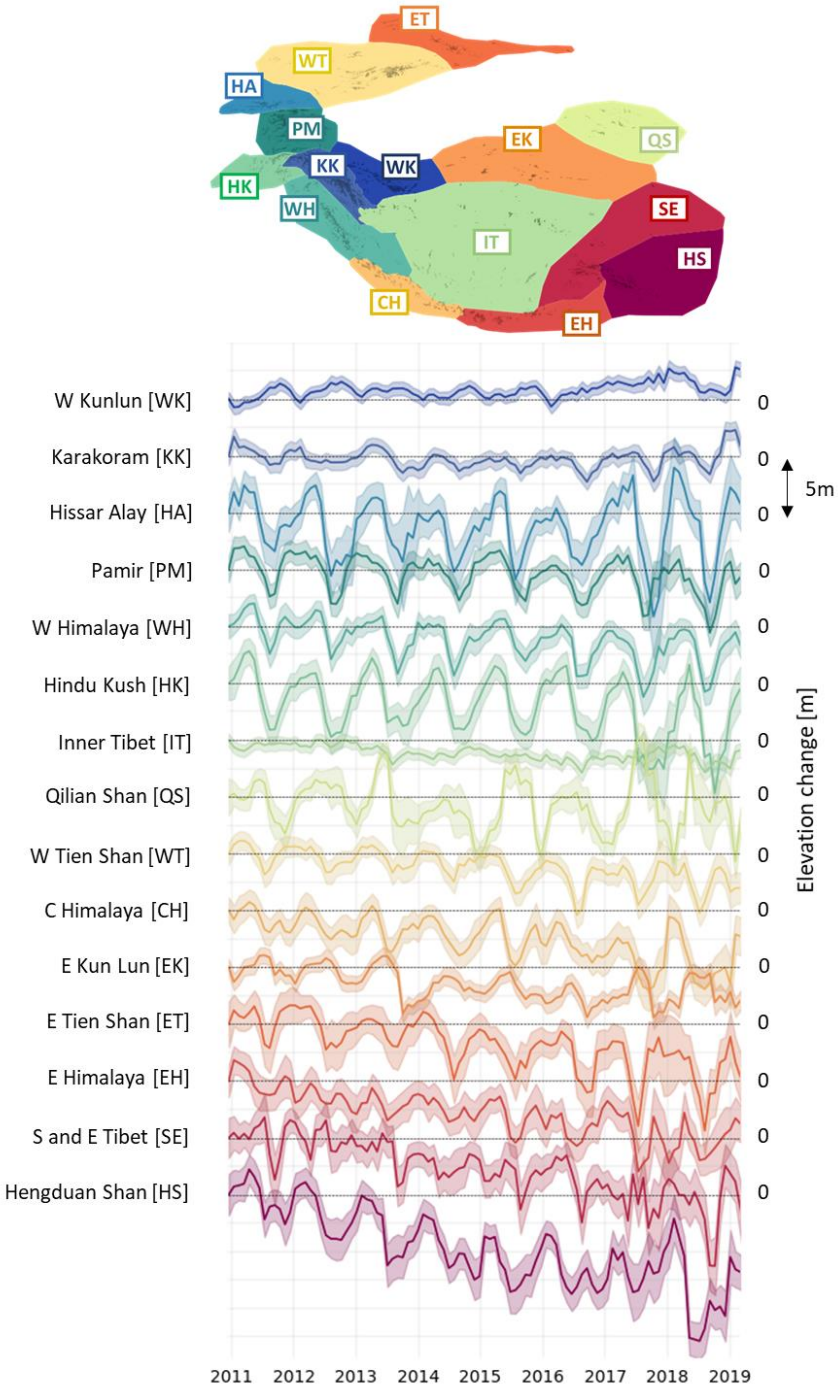

Figure S1: High Mountain Asia (HMA) monthly elevation change time series with uncertainty envelopes on sub-regional level (RGI second order regions) sorted by rate of elevation change.

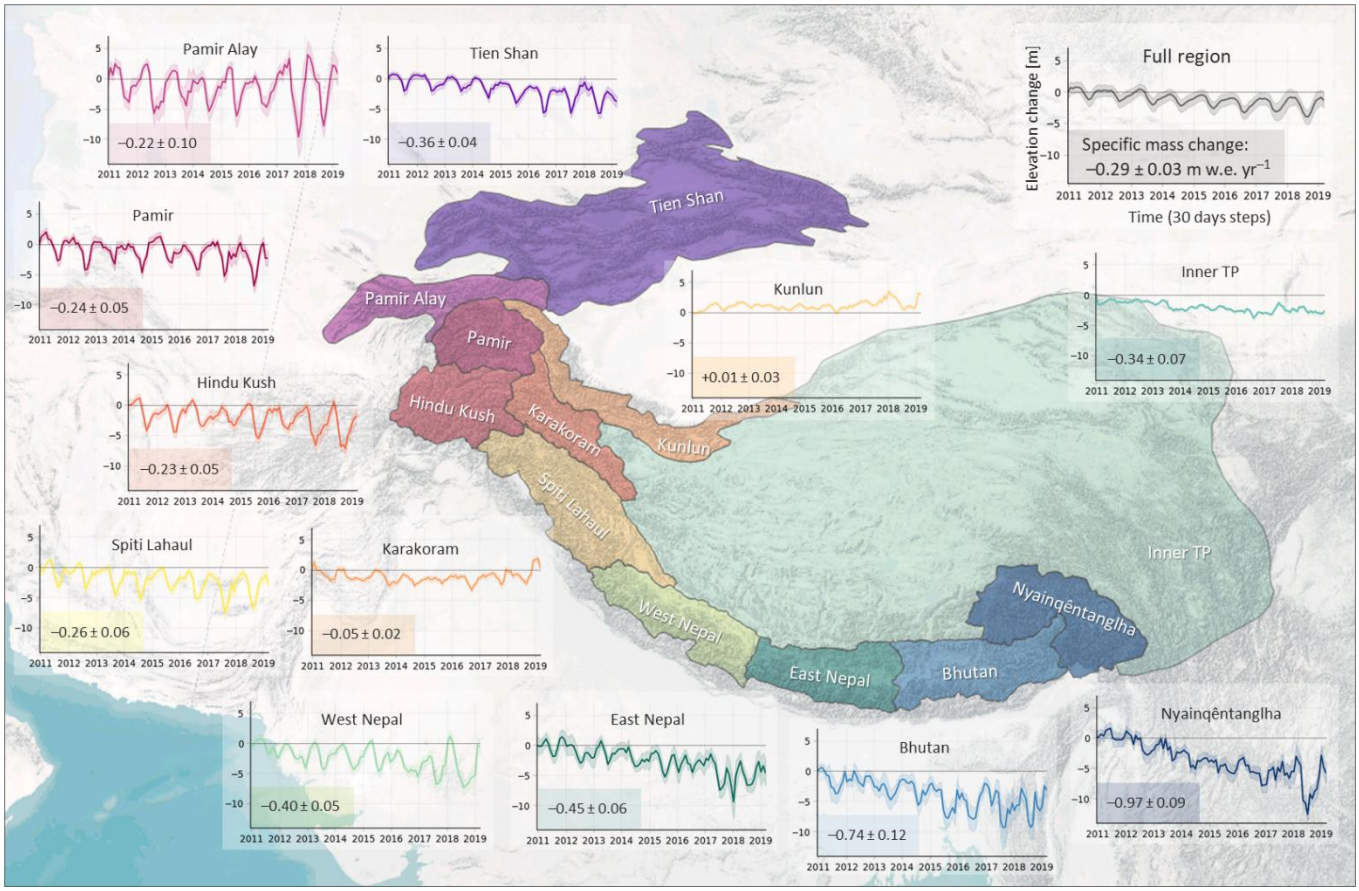

Figure S2: High Mountain Asia (HMA) 30-day elevation change time series on a sub-regional level using the mask by Brun et al. (2017). The coloured lines display the time series with the uncertainty envelope (*y-axis*: elevation change [m], *x-axis*: time [30-days steps]). The numbers describe the specific mass change with uncertainties in m w.e. yr^{-1}.

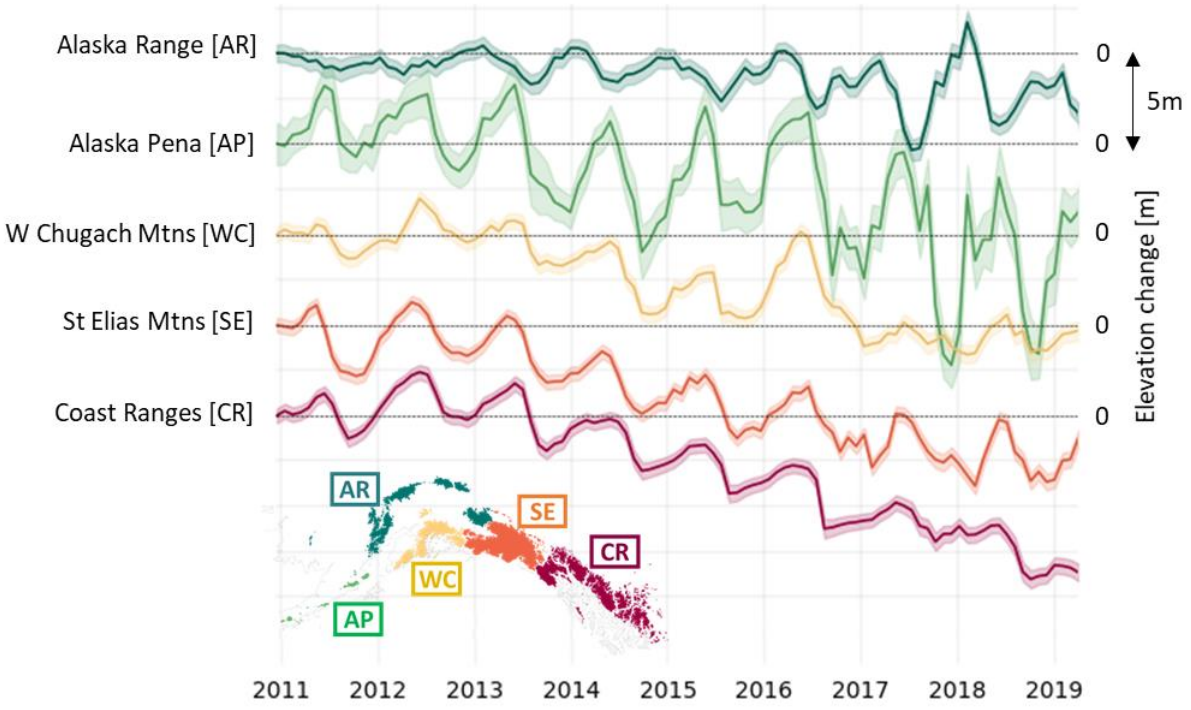

Figure S3: Gulf of Alaska (GoA) monthly elevation change time series on sub-regional level (RGI 6.0 second order regions) sorted by rate of elevation change.

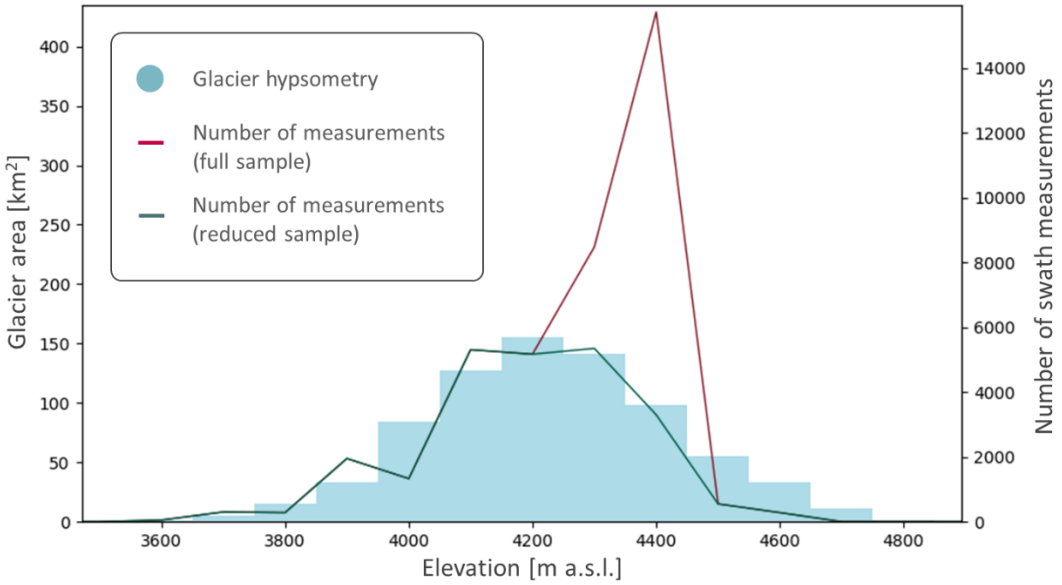

Figure S4: Illustration of elevation bias removal by sub-sampling for an example 100 x 100 km bin in High Mountain Asia. The light blue bars represent the glacier hypsometry within the bin *(y-axis, left)* and the red line *(y-axis, right)* displays the number of swath measurement of the full sample showing a bias towards higher elevations. After sequentially removing swath measurements based on measurement uncertainty to match the glacier hypsometry (using a 5% threshold) we achieve the swath elevation measurements distribution displayed as the green line *(y-axis, right)*. This procedure reduces potential biases in the altitudinal distribution of observations but also leads to a sample reduction.

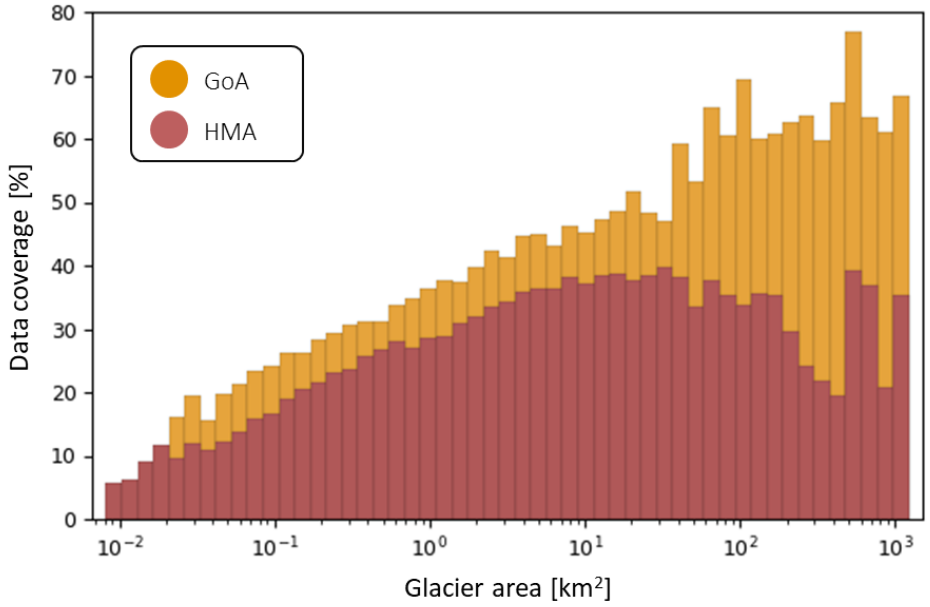

Figure S5: Relation between glacier size and CryoSat-2 swath elevation data coverage in High Mountain Asia and the Gulf of Alaska region.

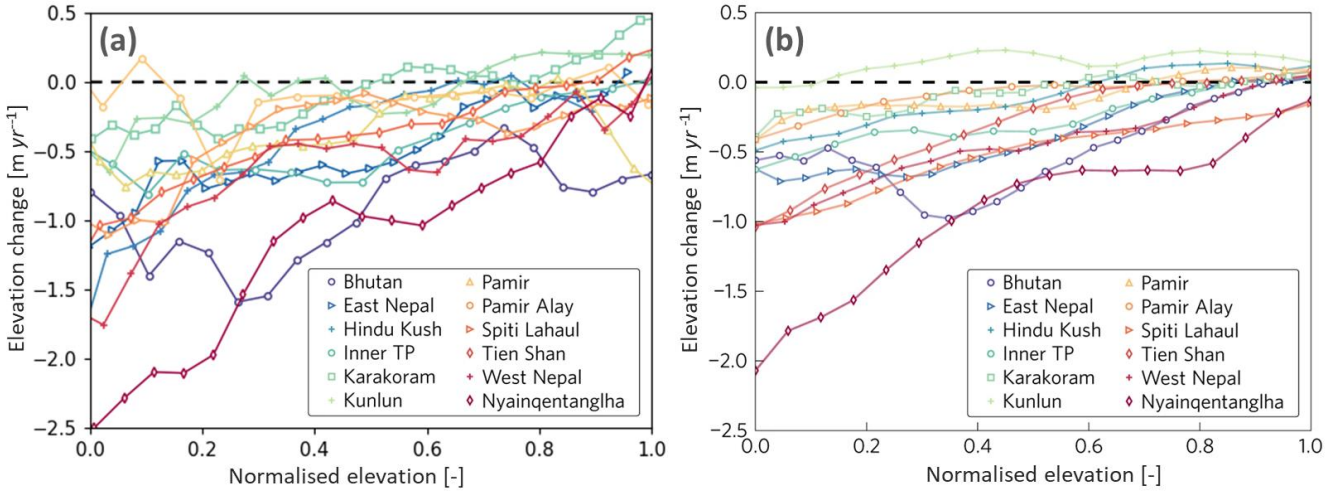

Figure S6: Elevation change rates in HMA (in 100 m elevation bins) as a function of normalised elevation from this study (a) in comparison with Brun et al. (2017) (b). To normalise elevation the formula $(z - z_{2.5})/(z_{97.5} - z_{2.5})$ is used, with z as elevation and $z_{2.5}$ as the elevation at 2.5 percentile of glacierised area and $z_{97.5}$ as the elevation at 97.5 percentile of glacierised area.

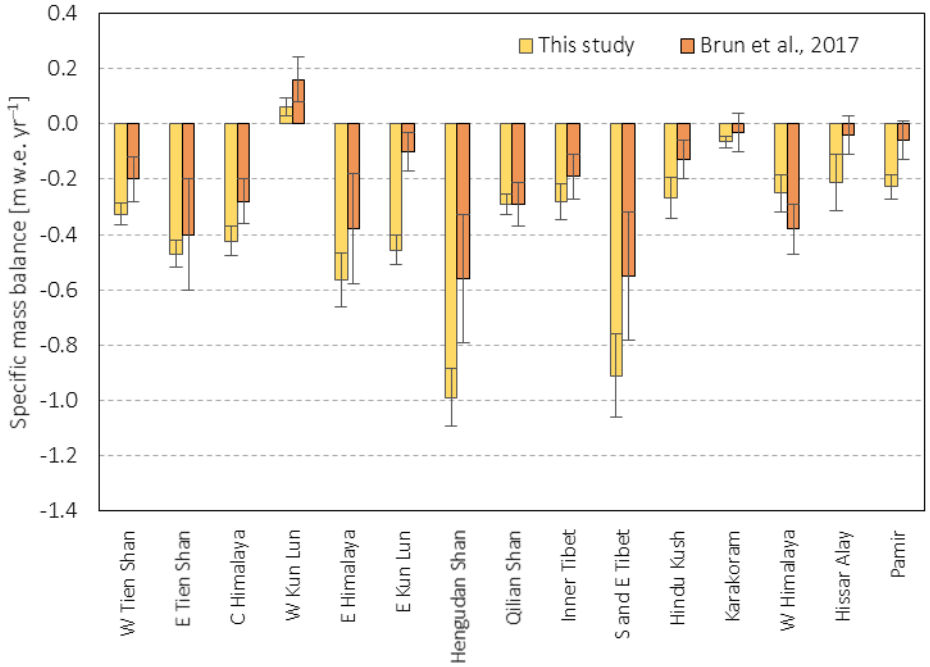

Figure S7: High Mountain Asia (HMA) specific mass balance trends on a sub-regional level (using the RGI 6.0 second order sub-region) in comparison with DEM differencing by Brun et al. (2017). This study covers the time period of 2010 to 2019, whilst Brun et al. (2017) cover the time period of 2000 to 2016.

3 Supplementary tables

	Glacier area [km^2]	This study [m w.e. yr^{-1}]	Shean et al., 2020 [m w.e. yr^{-1}]	Brun et al., 2017 [m w.e. yr^{-1}]	Kääb et al., 2015 [m w.e. yr^{-1}]
Inner TP	13537	–0.34 ± 0.07	–0.22 ± 0.05	–0.14 ± 0.07	–0.06 ± 0.06
Kunlun	10420	+0.01 ± 0.03	+0.04 ± 0.04	+0.14 ± 0.08	+0.18 ± 0.14
Pamir Alay	1917	–0.22 ± 0.10	–0.04 ± 0.09	–0.04 ± 0.00	–0.59 ± 0.27
Nyainqêntanglha	6944	–0.97 ± 0.09	–0.50 ± 0.15	–0.62 ± 0.23	–1.14 ± 0.58
East Nepal (Everest)	4980	–0.45 ± 0.06	–0.36 ± 0.09	–0.33 ± 0.20	–0.31 ± 0.14
Bhutan	2355	–0.74 ± 0.13	–0.55 ± 0.17	–0.42 ± 0.20	–0.76 ± 0.20
West Nepal	4657	–0.40 ± 0.05	–0.37 ± 0.09	–0.34 ± 0.09	–0.37 ± 0.15
Karakoram	20234	–0.05 ± 0.02	–0.04 ± 0.04	–0.03 ± 0.07	–0.09 ± 0.12
Spiti-Lahaul	7746	–0.26 ± 0.06	–0.31 ± 0.08	–0.37 ± 0.09	–0.42 ± 0.26
Pamir	7095	–0.24 ± 0.05	–0.11 ± 0.04	–0.08 ± 0.07	–0.41 ± 0.24
Hindu Kush	5326	–0.23 ± 0.05	–0.09 ± 0.06	–0.12 ± 0.07	–0.42 ± 0.18
Tien Shan	12099	–0.36 ± 0.04	–0.29 ± 0.07	–0.28 ± 0.20	–0.37 ± 0.31
Total	97310				

Table S1: High Mountain Asia (HMA) specific mass balance trends on a sub-regional level in comparison with DEM differencing and ICESat studies. It is important to note that Shean et al. (2020) cover the time period of 2000 to 2018, Brun et al. (2017) cover the time period of 2000 to 2016 and Kääb et al. (2015) cover the time period 2003 to 2008, whilst this study covers the time period of 2010 to 2019. We have complemented the data from Kääb et al. (2015) with ICESat data from Brun et al. (2017) for the sub-regions Kunlun, Inner TP, Tien Shan and Pamir Alay, which extended the estimates of Kääb et al. (2015) using the same method.

	$\boldsymbol{d}$	$\boldsymbol{c}$	$\boldsymbol{b}$	a	$\boldsymbol{d_{err}}$	c_{err}	$\boldsymbol{b_{err}}$
Alaska Range (Wrangell/Kilbuck)	-3.008926357	0.001859164	-2.40E-07	0	0.020969151	-0.000015343	3.43E-09
Alaska Pena (Aleutians)	-6.293731373	0.010054900	-5.09E-06	8.01E-10	0.086787480	-0.000181579	9.20E-08
West Chugach Mountains (Talkeetna)	-4.678348693	0.004822413	-1.67E-06	1.95E-10	0.013348888	-0.000017687	6.00E-09
Saint Elias Mountains	-3.463044478	0.002119418	-3.19E-07	0	0.011000255	-0.000016267	4.88E-09
Northern Coast Ranges	-3.224674716	0.001212905	0	0	0.016748088	-0.00002028	6.24E-09

Table S2: Polynomial coefficients describing the altitudinal distribution of elevation change rates $\sigma_{\Delta h}(k)$ and their corresponding errors $\sigma_{\Delta h\_err}(k)$ in the Alaska RGI 6.0 second order regions calculated from CryoSat-2 swath elevations between 2010 and 2019. Elevation changes in relation to altitude [m yr^{-1}] are described as one to three order polynomials $\sigma_{\Delta h}(k) = ak^3 + bk^2 + ck + d$ and the corresponding errors [m yr^{-1}] are described as two order polynomials $\sigma_{\Delta h\_err}(k) = b_{err}k^2 + c_{err}k + d$ with k representing the elevation in m a.s.l.

	$\boldsymbol{d}$	$\boldsymbol{c}$	$\boldsymbol{b}$	a	$\boldsymbol{d_{err}}$	c_{err}	$\boldsymbol{b_{err}}$
W Tien Shan	-5.430894095	0.001733559	-1.27E-07	0	0.720746599	-0.000317986	3.52E-08
E Tien Shan	17.85412608	-0.015099888	3.83E-06	-3.00E-10	2.319628442	-0.001166496	1.47E-07
C Himalaya	-69.60125902	0.037561058	-6.87E-06	4.23E-10	1.262957906	-0.000455633	4.12E-08
W Kun Lun	-2.139410906	0.000369918	0	0	1.270803238	-0.000422618	3.51E-08

E Himalaya	5.85068851	-0.002646660	2.62E-07	0	1.480776241	-0.000493023	4.13E-08
E Kun Lun	24.04975963	-0.010042428	1.01E-06	0	3.657901747	-0.00129725	1.15E-07
Hengduan Shan	22.94585098	-0.018957305	4.50E-06	-3.33E-10	2.319262315	-0.000949568	9.75E-08
Qilian Shan	75.33063669	-0.047931962	9.89E-06	-6.65E-10	6.115713322	-0.002381989	2.32E-07
Inner Tibet	-36.98988913	0.011858705	-9.51E-07	0	4.028370667	-0.001358846	1.14E-07
S and E Tibet	-11.77499997	0.003139844	-2.01E-07	0	0.248414888	-0.000068618	4.89E-09
Hindu Kush	-45.56736806	0.025203846	-4.78E-06	3.10E-10	2.194926188	-0.000874117	8.72E-08
Karakoram	-0.242945069	-0.000234290	5.03E-08	0	0.170047737	-0.000064542	6.37E-09
W Himalaya	-2.081792054	0.000335344	0	0	0.825667399	-0.000298594	2.71E-08
Hissar Alay	-0.608265349	0.000113994	0	0	1.228736870	-0.000578951	6.90E-08
Pamir	51.55194542	-0.035473036	7.90E-06	-5.73E-10	0.439495691	-0.000176018	1.80E-08

Table S3: Polynomial coefficients describing the altitudinal distribution of elevation change rates $\sigma_{\Delta h}(k)$ and their corresponding errors $\sigma_{\Delta h\_err}(k)$ in the High Mountain Asia RGI 6.0 second order regions calculated from CryoSat-2 swath elevations between 2010 and 2019. Elevation changes in relation to altitude [m yr^{-1}] are described as one to three order polynomials $\sigma_{\Delta h}(k) = ak^3 + bk^2 + ck + d$ and the corresponding errors [m yr^{-1}] are described as two order polynomials $\sigma_{\Delta h\_err}(k) = b_{err}k^2 + c_{err}k + d$ with k representing the elevation in m a.s.l.

4 References

Berthier, E., Schiefer, E., Clarke, G. K. C., Menounos, B. and Rémy, F.: Contribution of Alaskan glaciers to sea-level rise derived from satellite imagery, Nat. Geosci., 3(2), 92–95, doi:10.1038/ngeo737, 2010.

Berthier, E., Vincent, C., Magnússon, E., Gunnlaugsson, Á. Þ., Pitte, P., Le Meur, E., Masiokas, M., Ruiz, L., Pálsson, F., Belart, J. M. C. and Wagnon, P.: Glacier topography and elevation changes derived from Pléiades sub-meter stereo images, The Cryosphere, 8(6), 2275–2291, doi:10.5194/tc-8-2275-2014, 2014.

Brun, F., Berthier, E., Wagnon, P., Kääb, A. and Treichler, D.: A spatially resolved estimate of High Mountain Asia glacier mass balances from 2000 to 2016, Nat. Geosci., 10(9), 668–673, doi:10.1038/ngeo2999, 2017.

Gourmelen, N., Escorihuela, M., Shepherd, A., Foresta, L., Muir, A., Garcia-Mondejar, A., Roca, M., Baker, S. and Drinkwater, M. R.: CryoSat-2 swath interferometric altimetry for mapping ice elevation and elevation change, Adv. Space Res., doi:10.1016/j.asr.2017.11.014, 2018.

Huss, M.: Density assumptions for converting geodetic glacier volume change to mass change, The Cryosphere, 7(3), 877–887, doi:10.5194/tc-7-877-2013, 2013.

Moholdt, G., Hagen, J. O., Eiken, T. and Schuler, T. V.: Geometric changes and mass balance of the Austfonna ice cap, Svalbard, The Cryosphere, 4(1), 21–34, doi:10.5194/tc-4-21-2010, 2010a.

Moholdt, G., Nuth, C., Hagen, J. O. and Kohler, J.: Recent elevation changes of Svalbard glaciers derived from repeat track ICESat altimetry, Remote Sens. Environ., 114(11), 2756–2767, doi:10.1016/j.rse.2010.06.008, 2010b.

Nilsson, J., Sandberg Sørensen, L., Barletta, V. R. and Forsberg, R.: Mass changes in Arctic ice caps and glaciers: implications of regionalizing elevation changes, The Cryosphere, 9(1), 139–150, doi:10.5194/tc-9-139-2015, 2015.

Nuth, C., Moholdt, G., Kohler, J., Hagen, J. O. and Kääb, A.: Svalbard glacier elevation changes and contribution to sea level rise, J. Geophys. Res. Earth Surf., 115(F1), doi:10.1029/2008JF001223, 2010.

Pfeffer, W. T., Arendt, A. A., Bliss, A., Bolch, T., Cogley, J. G., Gardner, A. S., Hagen, J.-O., Hock, R., Kaser, G., Kienholz, C., Miles, E. S., Moholdt, G., Mölg, N., Paul, F., Radić, V., Rastner, P., Raup, B. H., Rich, J., Sharp, M. J. and Consortium, T. R.: The Randolph Glacier Inventory: a globally complete inventory of glaciers, J. Glaciol., 60(221), 537–552, doi:10.3189/2014JoG13J176, 2014.

RGI Consortium: Randolph Glacier Inventory – A Dataset of Global Glacier Outlines: Version 6.0, Technical Report, Global Land Ice Measurements from Space, Digit. Media, doi:10.7265/N5-RGI-60, 2017.

Shean, D. E., Bhushan, S., Montesano, P., Rounce, D. R., Arendt, A. and Osmanoglu, B.: A Systematic, Regional Assessment of High Mountain Asia Glacier Mass Balance, Front. Earth Sci., 7, doi:10.3389/feart.2019.00363, 2020.